Global vegetation patterns of the past 140,000 years

Received: 5 November 2019 | Revised: 11 May 2020 | Accepted: 18 May 2020

DOI: 10.1111/jbi.13930

RESEARCH PAPER

Journal of Biogeography | WILEY

Global vegetation patterns of the past 140,000 years

Judy R. M. Allen[1] | Matthew Forrest[2] | Thomas Hickler[2] | Joy S. Singarayer[3] | Paul J. Valdes[4] | Brian Huntley[1]

[1]Department of Biosciences, Durham University, Durham, UK

[2]Senckenberg Biodiversity and Climate Research Centre, Frankfurt am Main, Germany

[3]Department of Meteorology, University of Reading, Reading, UK

[4]School of Geographical Sciences, University of Bristol, Bristol, BS8 1SS, UK

Correspondence
Brian Huntley, Department of Biosciences, Durham University, South Road, Durham DH1 3LE, UK.
Email: brian.huntley@durham.ac.uk

Funding information
Leverhulme Trust, Grant/Award Number: RPG-2014-338

Handling Editor: Jack Williams

Abstract

Aim: Insight into global biome responses to climatic and other environmental changes is essential to address key questions about past and future impacts of such changes. By simulating global biome patterns 140 ka to present, we aimed to address important questions about biome changes during this interval.

Location: Global.

Taxon: Spermatophyta.

Methods: Using the LPJ-GUESS dynamic global vegetation model, we made 89 simulations driven using ice-core atmospheric CO_2 concentrations, Earth's obliquity, and outputs from a pre-industrial and 88 palaeoclimate experiments run using HadCM3. Experiments were run for 81 time slices between 1 and 140 ka, seven 'hosing' experiments also being run, using a 1-Sv freshwater flux to the North Atlantic, for time slices corresponding to Heinrich Events H0–H6. Using a rule-based approach, based on carbon mass and leaf area index of the LPJ-GUESS plant functional types, the biome was inferred for each grid cell. Biomes were mapped, and the extent and total vegetation biomass of each biome, and total global vegetation biomass, estimated.

Results: Substantial changes in biome extents and locations were found on all vegetated continents. Although the largest magnitude changes were in Eurasia, important changes were seen in tropical latitudes and the Southern Hemisphere. Total global extent of most biomes varied on multi-millennial (orbital) time scales, although some (e.g. Tropical Raingreen Forest) responded principally to the c. 100-kyr glacial–interglacial cycle and others (e.g. Temperate Broad-leaved Evergreen Forest) mainly to the c. 20-kyr precession cycle. Many also responded to millennial contrasts between stadial ('hosing') and interstadial climates, with some (e.g. Tropical Evergreen Forest) showing stronger responses than to the multi-millennial changes.

Main conclusions: No two time slices had identical biome patterns. Even equivalent Holocene and last interglacial time slices, and the last and penultimate glacial maxima, showed important differences. Only a small proportion of global land area experienced no biome change since 140 ka; many places experienced multiple biome changes. These modelling experiments provided little evidence for long-term biome stability.

KEYWORDS
biomes, carbon mass, glacial, global palaeovegetation maps, HadCM3, Heinrich Events, interglacial cycle, LPJ-GUESS, millennial climatic fluctuations

1 | INTRODUCTION

A recent study of almost 600 palaeovegetation records concluded that climatic changes since the last glacial maximum (LGM) drove moderate-to-large changes in both the composition and structure of vegetation at most locations across the globe (Nolan et al., 2018). Vegetation modelling studies have reached similar conclusions, albeit they also emphasize the role of the increase in atmospheric carbon dioxide concentrations ($[CO_2]_{atm}$) since the LGM in driving observed vegetation changes (Prentice, Harrison, & Bartlein, 2011). Although such studies contrasting the LGM and recent past provide valuable insights into global vegetation changes across the past 21 kyr, both global climate and $[CO_2]_{atm}$ have fluctuated substantially, on time scales of 10^4–10^5 years, throughout at least the past 800 kyr (EPICA community members, 2004; Jouzel et al., 2007; Luthi et al., 2008), whilst climate has also exhibited strong centennial to millennial fluctuations (Rasmussen et al., 2014). Using the LPJ-GUESS dynamic vegetation model (Smith, Prentice, & Sykes, 2001; Smith et al., 2014), Huntley, Allen, Collingham, et al. (2013) showed the sensitivity of vegetation in higher latitudes of the Northern Hemisphere to the contrasts between simulated stadial and interstadial climates during the last glacial stage (Singarayer & Valdes, 2010). Other research has shown a strong correlation in southern Africa between high present diversity of endemic bird species and areas where the same biome was simulated to have persisted throughout the past 140 kyr (Huntley et al., 2016).

The objective of this study was to address a number of important questions relating to the global impacts upon vegetation of both the climatic changes of various magnitudes and the changes in $[CO_2]_{atm}$ that have taken place during the past 140 kyr, a period extending from the penultimate glacial maximum (PGM) through the last interglacial (LIG), the last glacial stage and the Holocene, to the present. Specific questions to be addressed were as follows: What was the magnitude of changes in the extent of forest biomes, especially in the tropics, across the last glacial–interglacial cycle? How extensive and persistent were the temperate and boreal non-forest biomes considered favourable for Pleistocene mega-herbivores? What was the nature and extent of vegetation responses in tropical latitudes and the Southern Hemisphere to last glacial stage millennial climatic fluctuations? How similar were LIG global vegetation patterns to those that characterize the Holocene? How similar were global vegetation patterns of the PGM and LGM? In order to achieve our objective, we used the LPJ-GUESS dynamic global vegetation model (DGVM; Smith et al., 2001, 2014) to simulate global vegetation for a series of time slices, 0–140 ka BP, for which climatic conditions had been simulated. The LPJ-GUESS simulations were used to infer the extent and location of a series of biomes for each time slice, allowing global palaeovegetation maps to be drawn, then analysed to address these questions.

2 | MATERIALS AND METHODS

2.1 | Palaeoclimate experiments

An internally consistent series of 88 palaeoclimate experiments, including seven 'hosing' experiments designed to mimic Heinrich Events H0–H6, in which a 1-Sv fresh water flux was added to the surface layer in the North Atlantic for 200 years, plus a pre-industrial experiment, were performed using the HadCM3 fully coupled atmosphere–ocean general circulation model (AOGCM). The design of the experiments followed Singarayer and Valdes (2010) with respect to the boundary conditions and forcings applied, but with two important exceptions. Firstly, rather than using a static pre-industrial land surface for all experiments, the AOGCM was coupled to Triffid (Cox, 2001), a simple DGVM with five plant functional types (PFTs), enabling the vegetation and climatically important landsurface properties (e.g. forest vs. grassland) to interact dynamically with the atmosphere. The precise model configuration is HadCM3B-M2.1aD, as defined in Valdes et al. (2017). Secondly, rather than using ice sheets of LGM extent but reduced elevation for pre-LGM time slices of the last glacial stage, and modern ice sheets not only for LIG time slices but also for pre-LIG time slices, more realistic representations of pre-LGM ice sheets were used. For pre-LGM time slices of the last glacial stage, ice-sheet configuration used the ICE-5G (Peltier, 2004) ice sheet for the post-LGM time slice with the closest matching eustatic sea-level depression. For LIG and pre-LIG time slices, ice sheets were specified following de Boer, van de Wal, Lourens, Bintanja, and Reerink (2013). More details of the model set-up can be found in Davies-Barnard, Ridgwell, Singarayer, and Valdes (2017).

For input to LPJ-GUESS, anomalies were calculated for each palaeoclimate experiment with respect to the pre-industrial experiment, in each case using the climatology of the last 30 years of the experiment (Singarayer & Valdes, 2010). Anomalies were required for the twelve monthly mean temperatures (°C), monthly precipitation totals (mm) and monthly mean cloud cover (%).

2.2 | LPJ-GUESS simulations

The LPJ-GUESS DGVM simulates the dynamics of stands of vegetation comprised of a series of PFTs defined by the user. PFTs that can coexist in a given climate compete for resources, their functional traits determining their competitive balance and, hence, their relative biomass and fractional cover. The fire module used here (Smith

et al., 2014; Thonicke, Venevsky, Sitch, & Cramer, 2001) simulates fire disturbance and its effects based on soil moisture (as a proxy for fuel moisture), fuel load and a PFT-specific fire resistance. In addition, a stand-replacing stochastic disturbance with pre-defined average return interval represents other disturbances, such as wind storms and pest attacks. As nitrogen deposition for past periods is uncertain, the model was run without the nitrogen cycle and nitrogen limitation (i.e. the C-only version of Smith et al., 2014). The vegetation of each cell of a 0.5 × 0.5° longitude × latitude grid, comprising all grid cells that had non-zero land area for at least one time slice, was simulated. Following Huntley, Allen, Barnard, Collingham, and Holliday (2013), the potential 1901–30 monthly mean temperature, monthly precipitation and monthly mean cloudiness of grid cells on shelf areas exposed by lowered glacial sea levels were estimated using thin-plate spline surfaces fitted to data for land grid cells in the CRU TS 3.0 dataset (Harris, Jones, Osborn, & Lister, 2014). Palaeoclimatic conditions for each grid cell, including those on shelf areas, were obtained following the approach of Miller et al. (2008). Anomalies derived from the palaeoclimate experiments were applied to the CRU TS 3.0 annual time series of climatic data for 1901–30, monthly mean temperature time series first being detrended to remove the warming trend seen over those three decades. This time series was then cycled through repeatedly as required. Atmospheric carbon dioxide concentration for each time slice was determined according to Vostok ice-core data (Loulergue et al., 2008; Petit et al., 1999) using the EDC3 chronology (Parrenin et al., 2007). Obliquity was specified following Laskar et al. (2004). Twenty PFTs were used (Table 1). Eleven tree and two grass PFTs were specified following Forrest

TABLE 1 Plant functional types

Acronym	Plant functional type
BNE	Boreal Needle-leaved Evergreen Tree
BINE	Shade-intolerant Boreal Needle-leaved Evergreen Tree
BNS	Boreal Needle-leaved Summergreen Tree
BIBS	Shade-intolerant Boreal Broad-leaved Summergreen Tree
TeNE	Temperate Needle-leaved Evergreen Tree
TeBS	Temperate Broad-leaved Summergreen Tree
TeIBS	Shade-intolerant Temperate Broad-leaved Summergreen Tree
TeBE	Temperate Broad-leaved Evergreen Tree
TrBE	Tropical Broad-leaved Evergreen Tree
TrIBE	Shade-intolerant Tropical Broad-leaved Evergreen Tree
TrBR	Tropical Broad-leaved Raingreen Tree
BESh	Boreal Evergreen Shrub
BSSh	Boreal Summergreen Shrub
TeESh	Temperate Evergreen Shrub
TeRSh	Temperate Raingreen Shrub
TeSSh	Temperate Summergreen Shrub
TrESh	Tropical Evergreen Shrub
TrRSh	Tropical Raingreen Shrub
C3G	C3 Grass
C4G	C4 Grass
	PFT Aggregates used in biome inference
B-tree	Sum of Boreal Trees (BNE + BINE + BNS + BIBS)
Te-tree	Sum of Temperate Trees (TeNE + TeBS +TeIBS + TeBE)
Tr-tree	Sum of Tropical Trees (TrBE + TrIBE +TrBR)
B-shrub	Sum of Boreal Shrubs (BESh + BSSh)
Te-shrub	Sum of Temperate Shrubs (TeESh + TeRSh +TeSSh)
Tr-shrub	Sum of Tropical Shrubs (TrESh + TrRSh)
BE_tree	Sum of Boreal Evergreen Trees (BNE + BINE)
BS_tree	Sum of Boreal Summergreen Trees (BNS + BIBS)
TeE_tree	Sum of Temperate Evergreen Trees (TeNE + TeBE)
TeS_tree	Sum of Temperate Summergreen Trees (TeBS + TeIBS)
TrE_tree	Sum of Tropical Evergreen Trees (TrBE + TrIBE)

et al. (2015), whilst seven shrub PFTs were newly defined. Attribute values for the shrub PFTs were estimated on the basis of information from the literature. Attribute specifications for all PFTs are given in Appendix S1.

For each grid cell, 25 replicate 0.1-ha stands were simulated. For each stand, the model was run for 590 simulated years; average return time for stand-destroying disturbances was 100 years. Grid cell values of vegetation attributes were computed as the overall mean of the mean simulated values for the last 90 years for the replicate stands. Simulations were made for each of the 88 time slices for which palaeoclimate experiment results were available, as well as for the 'present' (i.e. the pre-industrial experiment). For the latter, climate data for 1901–30 were used without application of any anomalies, atmospheric carbon dioxide concentration was 280 ppmv and obliquity specified at its contemporary value. Two variables computed by LPJ-GUESS were analysed for each PFT and for each 0.5° grid cell: vegetation biomass (carbon mass) and leaf area index (LAI). For carbon mass, grid cell totals for each PFT were computed using the estimated ice-free land area of the grid cell at that time (see Appendix S2).

2.3 | Biome inference

The biome for each 0.5° grid cell and during each time slice was inferred from the simulated values of LAI and carbon mass for the 20 PFTs. A total of 21 biomes was recognized (Table 2). Inference was performed using a series of rules applied sequentially (expressed in the form of a dichotomous key in Appendix 1) and implemented in a Fortran program written for the purpose (see Appendix S3). In addition to reporting the inferred biome for each grid cell, this program also reported for each time slice: the extent of each biome, both as a total area (km^2) and as percentage of ice-free land area; the number and percentage of grid cells with ice-free land assigned to each biome; and the total carbon mass (kg) for each biome. The global total of ice-free land area, number of grid cells with ice-free land and global total carbon mass were also calculated and reported for each time slice. For each biome, the total carbon mass of each PFT, and the percentage of the biome's total carbon mass contributed by each PFT, were also calculated and reported for each time slice.

Using maps of the simulated carbon mass and LAI for the present for the 20 PFTs and 11 PFT aggregates, as well as a map of total simulated carbon mass, and a proposed set of 19 biomes, the initial rule set was developed, guided principally by expectations as to which PFTs would characterize each biome, and applied. Whereas most biomes could be distinguished using LAI criteria for associated PFTs, a carbon mass threshold was needed to distinguish desert and tundra biomes from the remainder, the initial threshold value being assigned by inspection of the map of total simulated carbon mass. The resulting global distribution of simulated biomes was mapped and compared visually with published maps of simulated potential pre-industrial biomes (e.g. Prentice et al., 1992, 2011) and of present biomes inferred from remaining natural and semi-natural vegetation (e.g. Olson, Watts, & Allison, 1983; Olson et al., 2001). Discrepancies between the simulated and published biome distributions were then progressively minimized by iteratively tuning the criteria used in the rule set, re-applying the rules and mapping the resulting biome distribution. This process resulted in the addition of two further biomes to the set being inferred, and to the final carbon mass and LAI criteria used for assigning the 21 biomes (see Appendix 1). No quantitative assessment of the match to any particular published biome map was attempted, not only because none of these define or portray quite the same set of biomes, but, in addition, as Scheiter and Higgins (2009) showed, the accuracy of the match is strongly influenced by the choice of map with which to make the comparison.

TABLE 2 Simulated biomes

Acronym	Biome
Des	Desert
Se-des	Semi-desert
TrG	Tropical Grassland
Sav	Savanna
TrRF	Tropical Raingreen Forest
TrEF	Tropical Evergreen Forest
TeSh	Temperate Shrubland
WTeWo	Warm Temperate Woodland
TeBEF	Temperate Broad-leaved Evergreen Forest
TeSF	Temperate Summergreen Forest
TeNEF	Temperate Needle-leaved Evergreen Forest
TeMxF	Temperate Mixed Forest
TePk	Temperate Parkland
St	Steppe
BPk	Boreal Parkland
BENF	Boreal Evergreen Needle-leaved Forest
BSNF	Boreal Summergreen Needle-leaved Forest
BSBF	Boreal Summergreen Broad-leaved Forest
BWo	Boreal Woodland
ShT	Shrub Tundra
Tun	Tundra
UNC	Unclassified

Although all grid cells had a biome inferred for the 'present' simulation, a small number of grid cells (median 3, maximum 14, out of a median overall number of grid cells with ice-free land of 62,919) was unclassified for 81 of the 88 other time slices. The median areal extent of unclassified grid cells was 0.005% of global ice-free land area, with a maximum extent of 0.026% at 126 ka. Inspection of the simulated PFT profiles of unclassified grid cells revealed no consistent pattern with respect to their PFT composition; thus we concluded that they represent neither an additional no-analogue biome nor a consistent location in climatic space.

Global biome distributions were mapped for all time slices, with ice-sheet and ocean masks overlain onto each map, and the maps compiled as a slide show (see Supplementary Material Slideshow).

In addition, difference maps were drawn and transition matrices calculated for time slices compared when discussing the questions we sought to address [see Appendix S4 for description of method, difference maps (Figures S4.1–S4.26) and transition matrices (Tables S4.4–S4.29)].

3 | RESULTS

3.1 | Simulated present biomes

Tropical Evergreen Forest (TrEF– see Table 2 for all biome acronyms used below) is the most spatially extensive biome at present (Table 3; Figure 1), followed closely by Des, TrRF and TeSh. TrEF, however, makes substantially the largest contribution to global carbon mass, accounting for 37.76%, with the next largest contributor, TrRF, accounting for just 14.96% and only three other biomes exceeding 5% (TeBEF – 8.27%; BENF – 6.94%; TeSF – 6.14%).

TABLE 3 Ice-free land area and carbon mass of simulated present biomes

	Ice-free land area	Carbon mass	
Biome acronym	(Mm^2)	(Pg)	(% global total)
Des	15.5	1.88	0.28
Se-des	4.9	4.21	0.62
TrG	4.6	3.08	0.45
Sav	5.7	8.87	1.30
TrRF	14.0	102.00	14.96
TrEF	15.7	258.00	37.76
TeSh	13.4	25.10	3.68
WTeWo	2.6	6.56	0.96
TeBEF	7.9	56.50	8.27
TeSF	5.4	41.90	6.14
TeNEF	0.4	3.14	0.46
TeMxF	3.9	31.10	4.55
TePk	3.6	17.40	2.54
St	1.9	1.51	0.22
BPk	6.6	33.40	4.89
BENF	9.1	47.40	6.94
BSNF	0.5	1.49	0.22
BSBF	3.3	13.60	1.99
BWo	4.0	11.60	1.70
ShT	6.2	14.00	2.05
Tun	0.9	0.18	0.03
UNC	0.0	0.00	0.00
Total	130.1	683	100.00

3.2 | Impacts of orbitally forced climatic changes on global biome patterns and carbon mass

Biome distributions at 22, 10, 114 and 126 ka provide an opportunity to explore the effects of orbital-scale changes in insolation and climate on biome distributions and terrestrial carbon mass (Figure 2; see also Figures S4.1–S4.5 and Tables S4.4–S4.8 for difference maps and transition matrices). The first two time slices represent the Northern Hemisphere (55°N) last glacial minimum (22.4 ka) and Holocene maximum (9.7 ka) of summer (June 21st–July 20th) insolation, whilst the latter two represent the extreme minimum (114.7 ka) and maximum (125.4 ka), respectively, of Northern Hemisphere summer insolation since 140 ka.

Although global ice-free land area at 22 ka is almost identical to that today, ice-covered areas being almost exactly compensated for by exposed shelf areas, global total carbon mass at 22 ka is only 61.2% of that simulated for the present. This reflects more or less doubled extents of Des and ShT, an almost 7-fold increase in the extent of Tun, and substantial increases in the extent of St, TrG, Sav and WTeWo, all biomes with relatively low carbon mass per unit area, along with reduced extents of several biomes with relatively high carbon mass per unit area. TeMxF and TrRF both have c. 3-fold reductions in extent, TeSF is reduced to 38.5% and BENF is reduced 4-fold, whilst TrEF, the biome with the highest present carbon mass per unit area, is reduced by nearly 10%.

At 10 ka, despite the residual ice sheets, especially the Laurentide Ice Sheet in North America, global ice-free land area is almost 5% greater than today. More strikingly, global total carbon mass is 97.5% of that simulated for the present, and hence almost 60% greater than at 22 ka. This primarily reflects greater extents of TrEF (+6.1%) and TrRF (+5.4%), as well as slightly increased carbon mass per unit area of TeEF (+1.2%), compared to present.

Notwithstanding 114 ka corresponding to the extreme Northern Hemisphere summer insolation minimum, estimated ice-sheet extent is similar to that at 10 ka, and ice-free land area is c. 4% greater than today. Somewhat unexpectedly, global carbon mass is 101.2% of that simulated for the present, despite marginally smaller extents of TrEF (−0.9%) and TrRF (−1.9%) than present, and decreased carbon mass per unit area of both compared to present (TrEF −1.4%, TrRF −10.0%). Four temperate and boreal forest biomes (TeMxF, TeSF, TeBEF and BENF), that have higher carbon mass per unit area than at present, make important contributions to the higher global carbon mass, with TeMxF making a 56% greater contribution to global carbon mass than at present as a result of a combination of 38% greater extent and 76% higher carbon mass per unit area.

Ice-free land area at 126 ka also is greater than at present, by about 2.7%, whereas global carbon mass is only 90.8% of that simulated for today, principally due to reduced extents (TrEF −3.6%, TrRF −2.4%) and decreased carbon mass per unit area (TrEF −6.8%, TrRF −9.4%) of tropical forest biomes.

Comparing biome distributions for the four time slices (Figure 2) reveals striking differences; none are closely similar. The

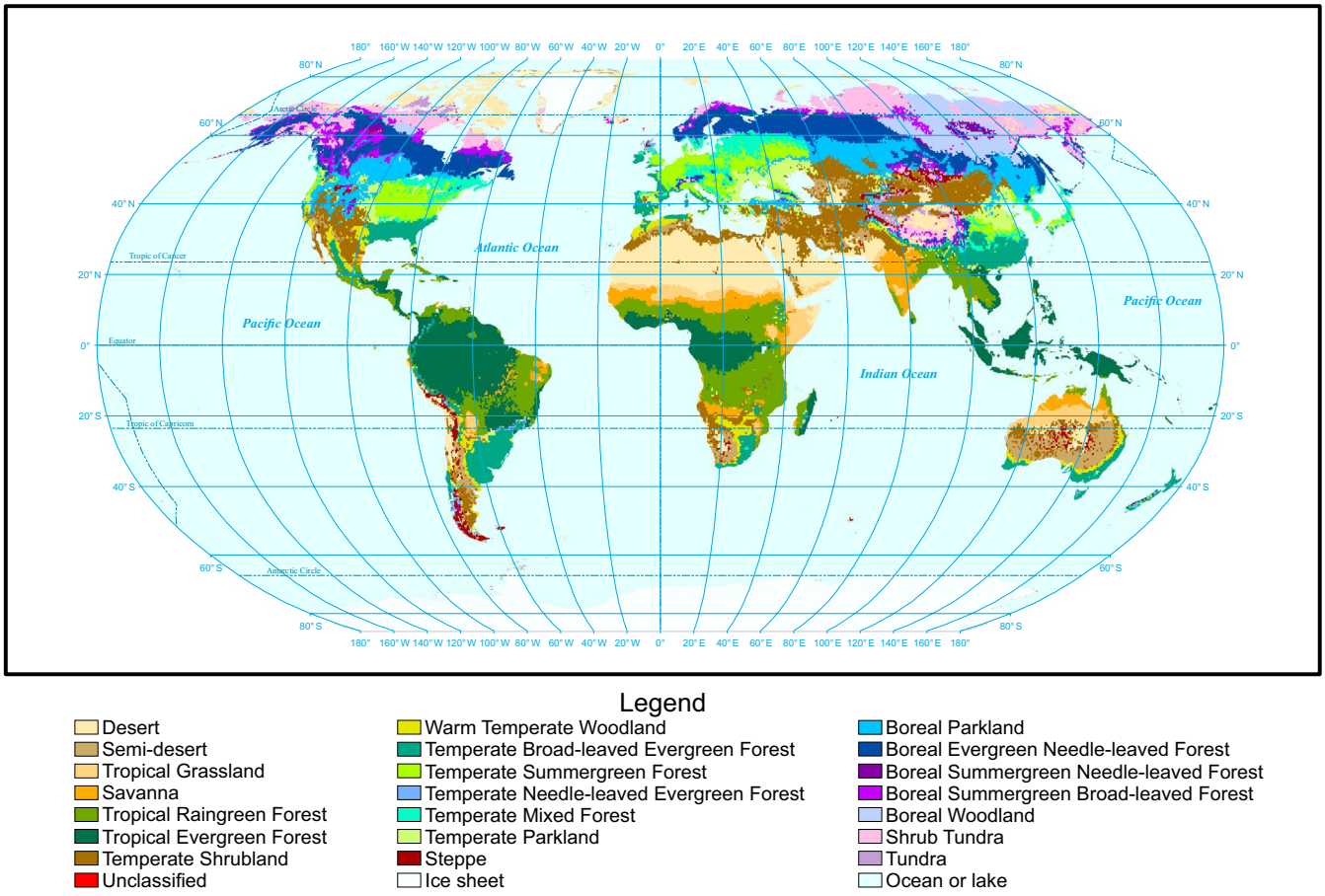

FIGURE 1 Simulated potential 'present' biome distribution. Global distribution of biomes inferred from an LPJ-GUESS simulation driven by early twentieth century (1901–30) climatic conditions, pre-industrial atmospheric carbon dioxide concentration of 280 ppmv and contemporary obliquity

most eye-catching differences are on the northern continents, especially Eurasia being dominated by Des, Tun and ShT at 22 ka, with very restricted extents of temperate and boreal forest biomes and a 78% increase in the extent of St. In contrast, the northern continents at the 114 ka insolation minimum are much more similar to present (Figure 1), except for northern North America, where the influence of the ice sheet is apparent, and north-eastern Eurasia, where forest biomes extend much further north than today. The patterns at 10 ka on the northern continents are again broadly similar to those today, although the extent of BENF is much reduced. The most similar patterns to today on the northern continents are at 126 ka, despite this being the peak insolation maximum and the present a modest insolation minimum.

Biome differences in tropical and southern latitudes are also important. In sub-Saharan Africa, Sav and TrRF extend substantially further north at the insolation maxima of 10 and 126 ka than they do at the minima of 22, 114 ka and today. South of the equator in Africa, areas occupied today by TrRF and Sav are at 22 ka simulated to be largely replaced by TeBEF and WTeWo, whereas at 114 ka differences from the present are much less striking. A similar contrast is seen between the insolation maxima, with 10 ka showing similar biome patterns in southern Africa to those at present, whereas at 126 ka the extent of WTeWo is markedly reduced and those of Sav and TrG are increased.

At 22 ka, areas in Central and northern South America occupied today by TrEF are instead occupied by TrRF or Sav, whereas much of the area of TrRF to the south of Amazonia today is replaced by TrEF. In addition, the western desert area is increased in extent, as is the area of WTeWo east of the Andes, whilst southernmost parts of the continent today supporting principally TeSh and St are occupied instead by ShT and Des. In contrast, at the 114 ka insolation minimum biome patterns in Central and South America are much more similar to those today, although with the extent of TrEF somewhat reduced, being replaced by TrRF in a belt along the Atlantic coast of Amazonia. At the 10 ka Northern Hemisphere insolation maximum, the extent of TrEF is increased, especially to the south of Amazonia where this biome occupies areas today supporting TrRF or Sav. The extent of WTeWo is also increased south of the Tropic of Capricorn, mostly into areas today occupied by TeBEF. Again, biome patterns at the 126 ka insolation maximum show a contrasting pattern of differences from those today. However, as at 10 ka, there is a greater extent of WTeWo and a reduced extent of TeBEF, and the extent of TrEF is decreased, with TrRF and Sav occupying increased areas.

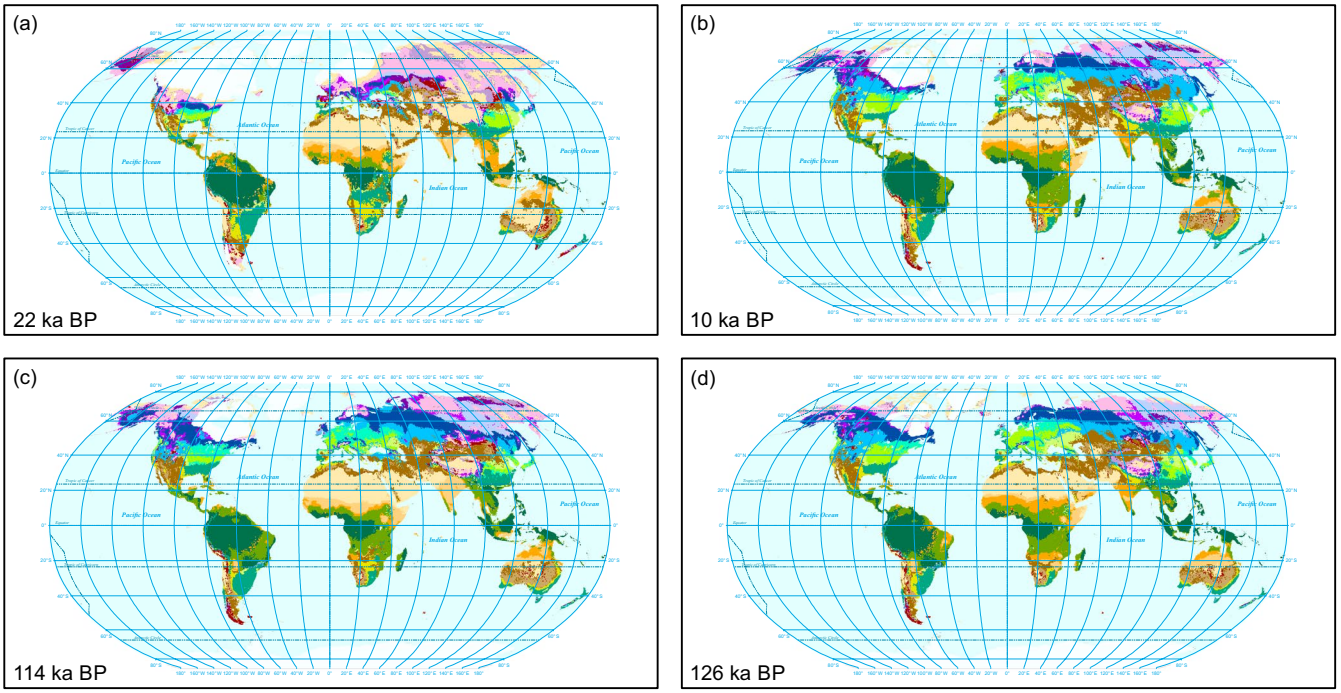

FIGURE 2 Simulated biomes for Northern Hemisphere summer insolation minima and maxima. Biomes inferred from LPJ-GUESS simulations driven by climate scenarios generated from palaeoclimate experiments for 22 ka (a), which is the time slice closest to the last glacial minimum of Northern Hemisphere summer insolation; 10 ka (b), which is the time slice closest to the early Holocene maximum of Northern Hemisphere summer insolation; 114 ka (c), which is the time slice closest to the most extreme minimum of Northern Hemisphere summer insolation since 140 ka; and 126 ka (d), which is the time slice closest to the most extreme maximum of Northern Hemisphere summer insolation since 140 ka. (Legend as in Figure 1)

In south-east Asia and Australasia, aside from striking changes in land–ocean configuration resulting from changes in global eustatic sea level, the most striking contrast with today is at 22 ka, when Sav is simulated to occupy large areas today supporting TrRF, TrG occupies much of the Indian sub-continent and the extent of Des in central Australia is very much greater than today. In contrast, biome patterns in the region at 114 ka are much more similar to those today, apart from on the Indian sub-continent where TrG occupies large areas today supporting Sav or TrRF. At 10 ka biome patterns are most similar to those today, the principal exception being the reduced extent of TrEF in eastern parts of the south-east Asian mainland that instead are occupied by an extension of the area of TrRF. Biome patterns at 126 ka are even more similar to those of the present.

3.3 | Impacts of last glacial stage millennial climatic fluctuations on global biomes

The last glacial stage is characterized by repeated alternations between relatively warm interstadials and severely cold stadials, as demonstrated by a range of Northern Hemisphere palaeoclimatic records spanning the last glacial stage and that have sufficient temporal resolution to record these centennial to millennial fluctuations (e.g. Allen et al., 1999; Allen, Watts, & Huntley, 2000). The magnitude and rate of climatic warming from stadials to succeeding interstadials are particularly clearly established for Greenland from ice-core data (Wolff, Chappellaz, Blunier, Rasmussen, & Svensson, 2010), with the most rapid and large magnitude warming episodes being associated with Heinrich Events (Andrews, 1998). Figure 3 (see also Figures S4.6–S4.11 and Tables S4.9–S4.14) presents biome maps for two time slices, 24 and 32 ka, corresponding to Heinrich Events H2 and H3. In each case biomes were simulated using the results from each of two palaeoclimatic experiments, the first, referred to hereafter as the 'normal' experiment, driven only by 'slow' forcings (orbital configuration, atmospheric greenhouse gas concentrations, ice-sheet configuration and land–ocean palaeogeography), and the second, designed to mimic the Heinrich Event and referred to as the 'hosing' experiment, additionally forced with a 1-Sv freshwater flux into the North Atlantic (Singarayer & Valdes, 2010).

For H2, which occurred at 24 ka close to the LGM minimum of Northern Hemisphere summer insolation, the contrast in biome patterns between the two experiments (Figure 3a,b) is striking, especially in Eurasia, where the extent of forest biomes (principally BENF, BSNF, BSBF and TeBEF) simulated for the normal experiment is very much greater than for the hosing experiment, forest biomes being almost entirely absent from western Europe for the latter (c.f. Huntley, Allen, Collingham, et al., 2013). Striking contrasts are also seen elsewhere around the globe, notably in Central America and northern South America, where large areas of TrEF and TrRF simulated for the normal experiment are replaced by Sav, TrG or Des in the hosing experiment. In sub-Saharan Africa, the extent of TrEF

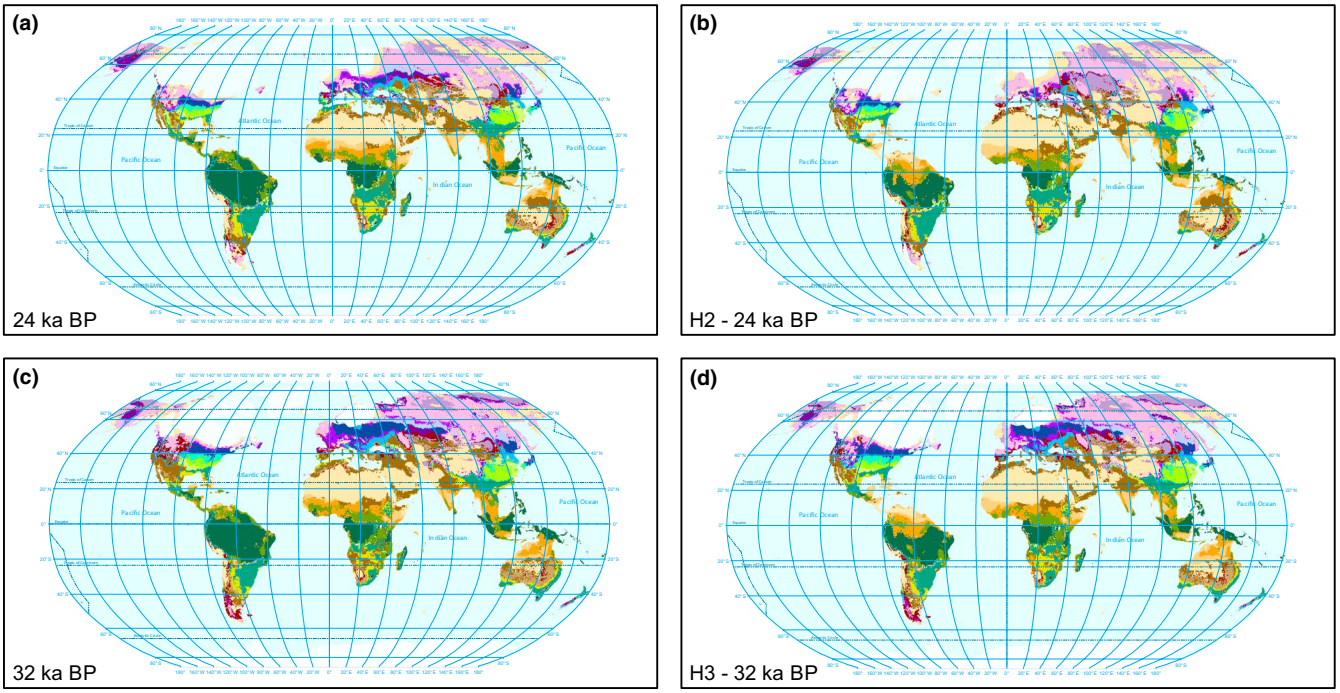

FIGURE 3 Simulated biomes for inter-stadial and stadial intervals of the last glacial stage. Biomes inferred from LPJ-GUESS simulations driven by climate scenarios generated from the 'normal' (a & c) and 'hosing' (b & d) palaeoclimate experiments for 24 ka (a & b) and 32 ka (c & d). Whereas the 'normal' experiments give climatic conditions corresponding to those of inter-stadials, the 'hosing' experiments, which are designed to mimic Heinrich Events H2 and H3, respectively, give stadial climatic conditions. (Legend as in Figure 1)

is less for the hosing experiment, as is the extent of Sav, whilst in the Indian sub-continent much of the area occupied by TrG for the normal experiment is Des for the hosing experiment. In South Africa, the continuous belt of TeBEF that extends from the Western Cape eastwards to the Mozambique border and beyond for the normal experiment is, for the hosing experiment, fragmented and replaced by WTeWo, Se-des and TePk. Similar more localized changes are seen in other regions, for example in Japan where ShT extends further south in the hosing experiment, mostly replacing BENF that in turn is shifted southwards, largely replacing TeMxF, the area of which is consequently reduced as it is squeezed against the southern coast.

In contrast to H2, H3 occurred close to a peak in Northern Hemisphere summer insolation at 33 ka. The 32 ka/H3 biome patterns (Figure 3c,d) differ much less than for 24 ka/H2, especially in Eurasia. Nonetheless, in the normal experiment, much of western Europe is simulated to have supported forest biomes, principally BSBF, with St towards the western fringes, whilst for the hosing experiment ShT dominates the region, with Tun and Des in the extreme west and north-west. Elsewhere, marked contrasts in biome patterns are seen in Central America and northern South America, and in sub-Saharan Africa, largely paralleling those seen for 24 ka/H2. In Australia, the normal experiment has a much smaller and fragmented area of Des in the centre of the continent than does either the normal or hosing experiment for 24 ka, whereas the area of Des is much increased in the H3 hosing experiment. The overall biome pattern in Australia at 32 ka also markedly differs from 24 ka, with a much reduced extent of TeSh and increased extents of TrG and Sav in the north.

3.4 | Holocene and last interglacial global biome patterns

Comparisons of the current and last interglacials test the degree to which biome distributions are similar or different between interglacial periods (Figure 4; see also Figures S4.12–S4.23 and Tables S4.15–S4.26). Whilst there are some clear parallels, there are also some striking differences. These differences partially reflect the longer duration of the LIG, for which we follow Brauer et al. (2007) who estimate the duration as 17.7 ± 0.2 kyr (127.2 to 109.5 ka), and thus c. 6 kyr longer than the Holocene. This longer duration means that by the end of the LIG, at 109.5 ka, Northern Hemisphere summer insolation had passed its minimum at 114.7 ka and had already increased by 34% of the difference between that minimum and the subsequent maximum at 103.1 ka. However, ice sheets are inferred to have been present in North America by the middle, and in Fennoscandia by the later millennia, of the LIG (Figure 4e,f), whereas no ice sheet was present in either area during later millennia of the Holocene.

Although there are obvious differences among all six maps presented in Figure 4, three are more similar, and also more similar to that for the present (Figure 1), namely those for 7 ka (Figure 4b), 3 ka (Figure 4c) and 126 ka (Figure 4d). Of these, the first two represent the mid- and late-Holocene (Walker et al., 2012), the first falling some 4,700 yr after the Holocene onset at 11.7 ka, whereas 126 ka is only 1,200 yr after the LIG onset, as dated by Brauer et al. (2007), and thus closest in timing relative to interglacial onset to the early Holocene time slice at 11 ka (Figure 4a). Notable differences include:

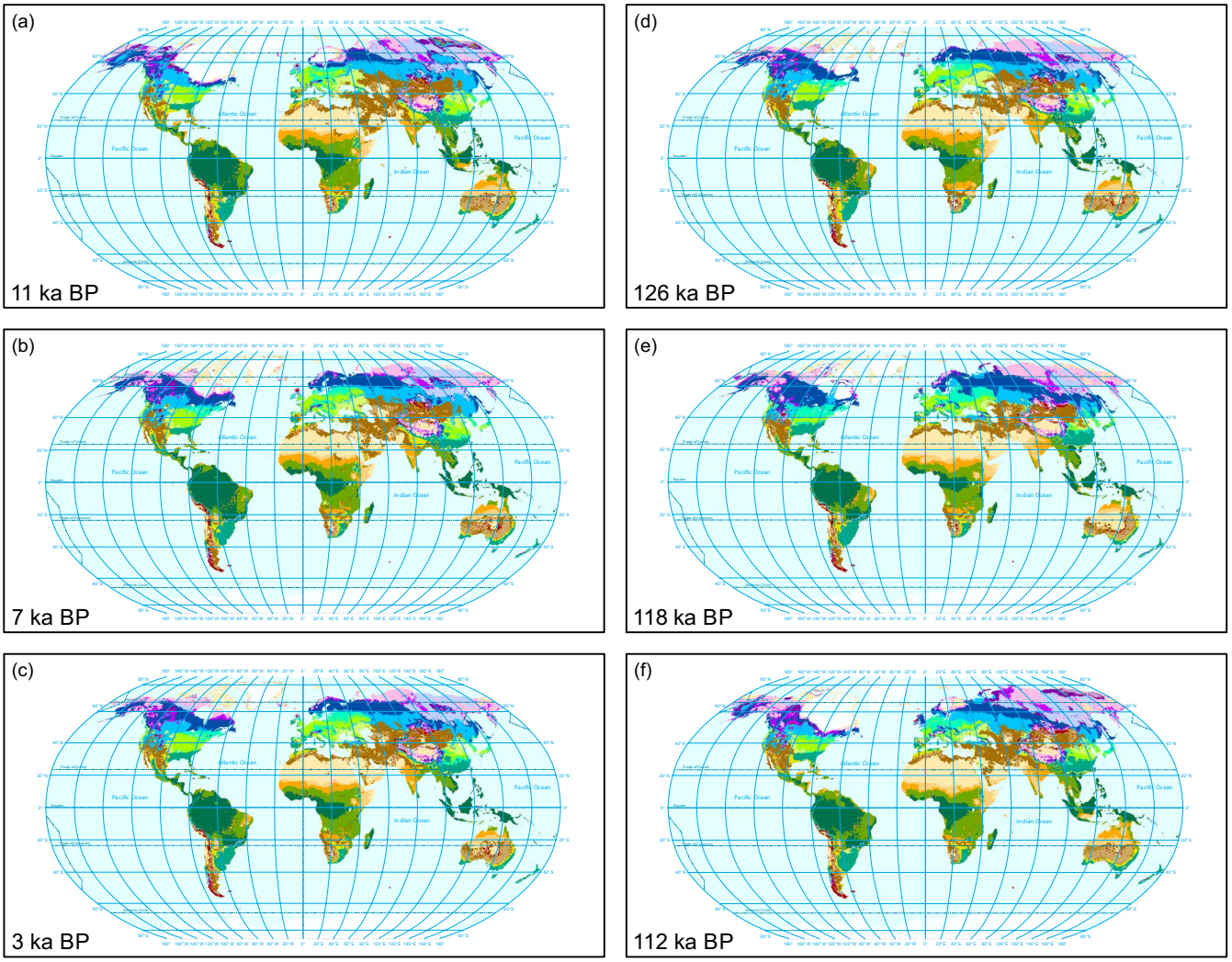

FIGURE 4 Simulated biomes for the Holocene and the last interglacial stage. Biomes inferred from LPJ-GUESS simulations driven by climate scenarios generated from palaeoclimate experiments for time slices representing early, middle and late in each of the Holocene and last interglacial: (a) 11 ka; (b) 7 ka; (c) 3 ka; (d) 126 ka; (e) 118 ka; and (f) 112 ka. (Legend as in Figure 1)

greater extent of the belt of TeBEF in eastern North America at 126 ka; more northerly location of the boundary between TeMxF and BENF in Europe at 126 ka; greater extent of ShT in western Siberia at 126 ka; smaller extent of Sav and greater extent of TrG south of the Sahara at 3 ka; and greater extent of TrG in Australia at 126 ka.

The other three biome distributions have substantial differences from the present (Figure 1), including the following:

- At 11 ka (Figure 4a), the extent of ShT in Siberia is much less than today, whereas BWo is more extensive and areas of BSNF, BSBF and BPk are simulated in northern Siberia well north of their northernmost areas simulated for the present. A similar more northerly extension of BSNF, BSBF, BENF and BPk is seen in Alaska. In sub-Saharan Africa, Sav extends further north than today, and TrG is less extensive south of the Sahara. WTeWo is more extensive in the north of the Indian sub-continent, whereas Sav and TrRF are both less extensive than today. In Australia, extents of Des, St and TeSh are less, and of Se-des greater, than today.
- At 118 ka (Figure 4e), ShT is more extensive in northern Eurasia than it is today, whereas BWo is much less extensive. BENF forms a more continuous belt across Eurasia, especially in the east, than today, as well as extending further north in northern Europe and western Siberia. In North America, the extent of BENF is greater than at present in the northern conterminous United States and Canada, mostly at the expense of BPk which is of much lesser extent. In the Indian sub-continent, TrRF is absent except in the south west, and the extent of Sav is reduced, and of TrG increased, compared to present. Sub-Saharan Africa and South America exhibit few striking differences from the present, whereas in Australia the extent of Des is much greater, and of TrG and Sav much less, than today.
- Global biome patterns at 112 ka BP (Figure 4f) are strikingly different from those today, and more similar to those at 11 ka than to those of any other LIG or Holocene time slice illustrated.

Notwithstanding this general similarity, there are nonetheless notable differences between biome patterns at 112 ka and at 11 ka. In Europe, BENF extends to the British Isles at 112 ka; the extent of TeSF is much less, and of TeMxF greater, than at 11 ka. In sub-Saharan Africa Sav is less extensive, with the belt south of the Sahara extending less far north and much reduced, whereas TrG is more extensive in that region, but again extends less far north, compared both to 11 ka and to today. In Central America and northern South America biome patterns are relatively similar at 112 ka to those at 11 ka, with a greater extent of Sav and less of TrEF than today, whereas further south in South America, and in Australia, 112 ka patterns are more similar overall to those at present. In the Indian sub-continent, the strongest similarity is to the biome patterns at 118 ka.

3.5 | Last and penultimate glacial maximum global biome patterns

Biome patterns for 21 ka, the time slice most frequently used to represent the LGM, and for 140 ka, used here to represent the PGM (Figure 5; see also Figures S4.24–S4.26 and Tables S4.27–S4.29)), both show marked differences from present biome patterns (Figure 1), as expected. Less expected, however, are marked differences between LGM and PGM biome patterns in many parts of the world. These include: temperate (TeSF, TeBEF, WTeWo, TeNEF) and Boreal (BSBF, BSNF, BENF, BWo) forest and woodland biomes are less extensive in Europe and western Siberia at the PGM than at the LGM, whereas Des, ShT and St are more extensive, especially in Europe; the PGM has greater extents of TeBEF and TeSh in the south-east and south-west, respectively, of North America, and of TrEF and TrRF in Central America and northern South America; in southern Amazonia and sub-Saharan Africa, TrEF is less, and TrRF more extensive at the PGM; and in southern Africa, TeBEF is less extensive and WTeWo and TeSh more extensive at the PGM.

3.6 | Global biome extents and carbon mass 140 ka to present

Over the last 140 ky, notable features of global biome distributions include the generally large extent of Des (Figure 6), with peak extents during the maxima of the penultimate and last glacial stages, and further increases in the Heinrich hosing simulations. Unsurprisingly, Tun and ShT, and to a lesser extent St, are also more extensive during glacials, and further increase in extent in Heinrich Event simulations. In contrast, TrRG, TeSF, TeMxF, BPk and BENF are most extensive during the Holocene and LIG, but show limited changes in global extent for Heinrich Event simulations. Several biomes show limited changes in global extent, most notably TrEF, although this biome exhibits marked decreases in extent under Heinrich simulations matched by marked increases in TrG. Several biomes tend to increase and decrease in extent associated with the precessionally driven peaks and troughs in Northern Hemisphere summer insolation (Figure 7), notably TeBEF, BPk, BENF and BSNF. However, some, for example TeBEF, have greater extents during insolation minima and others, for example BSNF, during insolation maxima.

Simulated global total carbon mass is highest during the Holocene and LIG, and reaches minimum values during the LGM and PGM (Figure 7). Overall changes in carbon mass are very similar to those calculated from the TRIFFID model by Davies-Barnard et al. (2017), although that study did not include the Heinrich events. Values are intermediate during most of the last glacial stage, but with strongly reduced values in simulations made for the Heinrich experiments. Several peak values correspond to minima in Northern Hemisphere summer insolation, although this pattern is not seen at the LGM and PGM, nor at the subdued insolation minimum centred on 41.8 ka. There is also a general correspondence between the changing $[CO_2]_{atm}$ and simulated global total carbon mass (Figure 7), although detailed comparison reveals that peak $[CO_2]_{atm}$ values do not generally correspond closely to peak global carbon mass. Thus, whilst changing $[CO_2]_{atm}$ almost certainly contributes to the 'first-order' pattern of changes in simulated carbon mass between glacial and interglacial conditions, the 'second-order' variations in carbon mass are more closely linked to insolation variation, and hence to consequent changes in global climatic conditions, perhaps especially in regions with strong climatic seasonality. Marked reductions in global carbon mass in simulations for Heinrich Event mimicking experiments represent an intriguing 'third-order' pattern of inverse relationship, the ice-core record showing $[CO_2]_{atm}$ rising to peak values coincident with Heinrich Events. This raises the possibility that these peaks in $[CO_2]_{atm}$ were driven at least in part, if not primarily, by releases of carbon from, and reduced carbon uptake by, global vegetation during Heinrich Events. The simulated median reduction in global carbon mass of 68.5 Pg (range 28–91 Pg) during Heinrich Events H0–H6 is more than sufficient to account for the increased $[CO_2]_{atm}$ recorded in ice-core data if this carbon was returned to the atmosphere, and such a source is also consistent with observed shifts in $\delta^{13}C$ of atmospheric CO_2 (Bauska et al., 2018).

4 | DISCUSSION

Visual comparisons showed general concurrence between our present biome distribution pattern and published global biome maps (e.g. Haxeltine & Prentice, 1996; Prentice et al., 2011). Similarly, visual comparisons of our past biome distributions with published palaeovegetation maps, whether derived from modelling (e.g. Guetter & Kutzbach, 1990; Prentice et al., 2011) or palaeovegetation data (e.g. Jolly et al., 1998; Marchant et al., 2009; Tarasov et al., 1998; Williams, Summers, & Webb, 1998), showed general concurrence of overall global patterns. Exceptions occurred mainly when comparing with biomes inferred from palynological data or derived from older palaeoclimate simulations using earlier vegetation models (e.g. BIOME 1, Prentice et al., 1992). Closest matches were with more recent DGVM studies (e.g. Prentice et al., 2011).

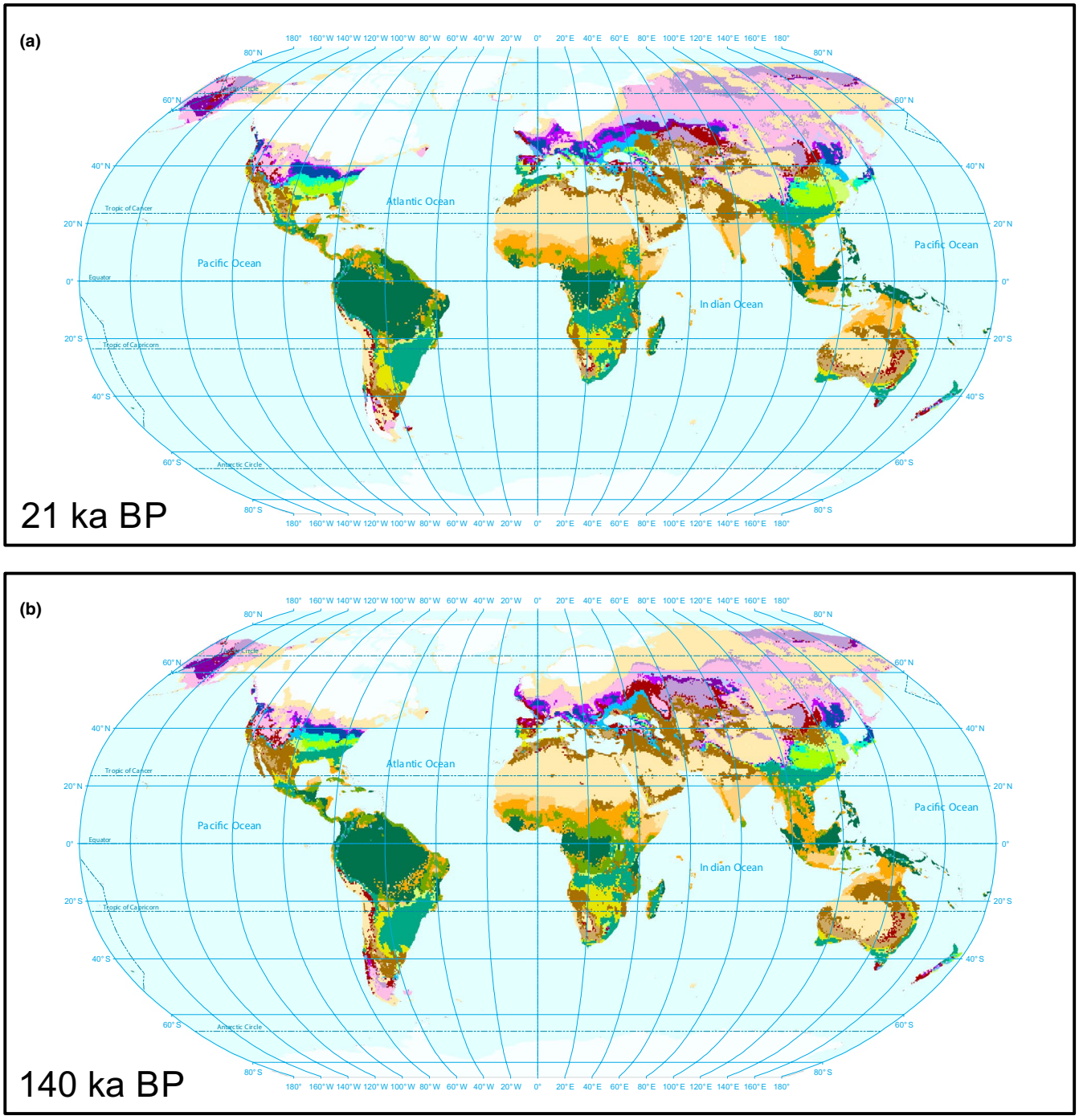

FIGURE 5 Simulated biomes for the last and penultimate glacial maxima. Biomes inferred from LPJ-GUESS simulations driven by climate scenarios generated from palaeoclimate experiments for 21 ka (a), generally taken as the last glacial maximum, and 140 ka (b), a time slice close to the penultimate glacial maximum. (Legend as in Figure 1)

As stated in Section 1, our study aimed to address several questions. The first related to the magnitude of changes in the extent of forest biomes, especially in the tropics, over the last glacial–interglacial cycle. Prentice et al. (2011) simulated a ratio of 1.2 between the present and LGM extents of Tropical Forest, whereas we simulate a ratio of 1.6 between the present and 21 ka extents of TrEF + TrRF. Our simulations spanning the entire glacial–interglacial cycle, including those for climatic conditions produced by climate model experiments designed to mimic Heinrich Events, give a ratio of 2.1 between the maximum extent, at 11 ka, and minimum extent, for the H1-mimicking simulation at 17 ka, of TrEF + TrRF. For temperate forests (TeMxF + TeSF + TeBEF), our simulations give a maximum-to-minimum extent ratio of 1.5, and for Boreal forests (BENF + BSNF + BSBF) of 3.9. The minimum extent of the former

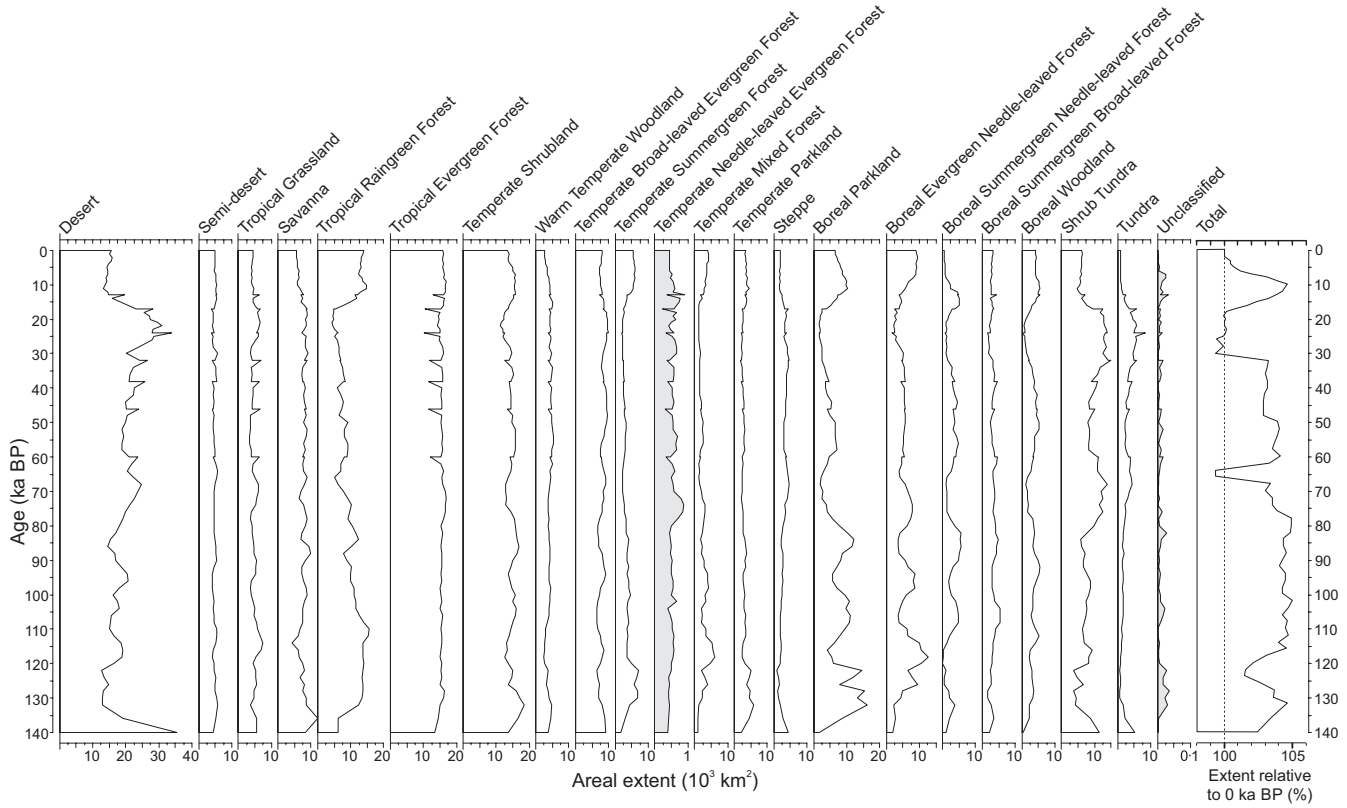

FIGURE 6 History of global extents of simulated biomes since 140 ka. Time series, 140 ka to present, of the simulated global areal extent of each biome, and the total extent of ice-free land expressed relative to that at present, are shown by the series of graphs. (Note: The horizontal scales of the shaded graphs for Temperate Needle-leaved Evergreen Forest and Unclassified differ from those of the remainder, the former by a factor of 0.1 and the latter by 0.01)

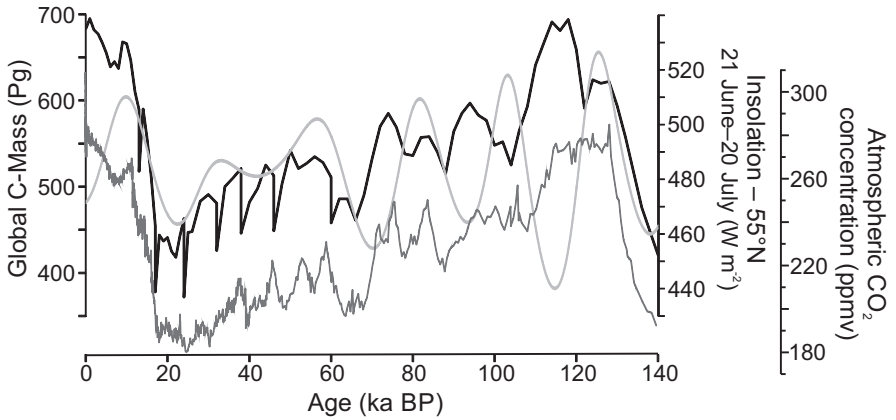

FIGURE 7 Simulated global carbon mass 140 ka to present. Total global carbon mass (heavy black line) simulated by LPJ-GUESS for the 88 palaeoclimate time slices and for the 'present'. For comparison, the summer (21st June–20th July) insolation at 55° N (smooth light grey line), computed following Laskar (2004), and atmospheric carbon dioxide concentration (dark grey line), following Bereiter et al. (2015; data downloaded 3rd October 2019 from http://ncdc.noaa.gov/paleo/study/17975), are also shown

was simulated for 60 ka and of the latter for H2 (24 ka); maximum extents of both were simulated for 118 ka. Thus, our results indicate that forests everywhere have experienced moderate-to-substantial changes in global extent over the last 140 kyr. In terms of their biodiversity legacy, changing extents of tropical forests may be of the greatest importance; it is noteworthy that TrRF experienced greater changes in extent (maximum-to-minimum extent ratio 3.53) than did the more diverse TrEF (maximum-to-minimum extent ratio 1.65). Similarly, the three categories of temperate forest show markedly different maximum-to-minimum ratios, the highest being for TeMxF (6.10). The ratio of 3.95 for TeSF may have a significant biodiversity legacy, whilst that of 1.54 for TeBEF, the most globally extensive temperate forest biome, may at least in part account for its generally higher species richness than that of TeSF. The most extreme ratio

of maximum-to-minimum global extent, a value of 206, is seen for the generally least extensive of the Boreal forest biomes, BSNF, its minimum extent being reached at 120 ka and its maximum at 86 ka. BENF, the Boreal forest biome with the greatest median extent, reached its minimum extent at H2 (24 ka) and its maximum at 118 ka, with a ratio of 7.46, whilst BSBF, with a ratio of 3.07, reached its minimum extent at 130 ka and its maximum at 108 ka. Thus, although forests everywhere experienced changes in extent since 140 ka, the magnitude of these changes varies considerably and there are strong indications that biomes that experienced smaller past changes in extent support greater biodiversity today.

Our second question concerned the extent and persistence of temperate and boreal non-forest biomes with which Pleistocene mega-herbivores are generally considered to have been associated. Of temperate and boreal biomes, Tun and St are generally dominated by the C3 Grass (C3G – see Table 1 for PFT acronyms) PFT, with limited components of tree and/or shrub PFTs. Both have greater simulated last glacial than Holocene or LIG extents (Figure 6); Tun had its greatest extent under the H2 (24 ka) climate and St under the 32 ka climate, whilst both had minimum extent under the 122 ka climate. However, extent alone tells only part of the story; simulated C3G carbon mass per unit area also shows systematic patterns of change in these biomes since 140 ka. For Tun this was markedly greater during the penultimate glacial and most of the last glacial stage, the exception being the millennia around the LGM, whereas for St it was consistently less during glacials than during either the Holocene or LIG. Together with the changes in extent, this results in Tun holding >20% of the C3G carbon mass present in the two biomes for most of the last glacial, rising to >25% in simulations for most time slices between 16 and 64 ka, and to peaks of >35% in those for H1, H2, H3 and 140 ka. In contrast, Tun generally holds <15% of the C3G carbon mass of the two biomes during the Holocene and LIG, falling to minima of c. 10%–11% during both interglacials. Overall, C3G carbon mass simulated for these biomes was generally markedly greater during the glacials, and had minimum values during earlier millennia of the LIG. Thus, whilst the marked reduction in herbaceous plant material biomass in these biomes simulated after the LGM corresponds to the principal period of decline, and in some cases eventual extinction, of grazing specialists among the Pleistocene mega-herbivores of the northern continents, their persistence during the LIG when simulated herbaceous plant biomass in these biomes reached minimum values appears anomalous. However, fossil evidence of LIG presence of Pleistocene mega-herbivores has been reported from north-eastern Siberia, where evidence from fossil beetle assemblages, as well as palaeovegetation evidence, indicates the vegetation remained relatively open, with a smaller proportion of tall woody components than during the Holocene (Sher, 1997). Our simulations parallel this pattern; both total carbon mass and LAI of boreal tree PFTs (Sum of Boreal Trees – B-tree) are much less over eastern Siberia during the early LIG, when C3G carbon mass of Tun and St was at a minimum, than in the present simulation. Recent evidence from analyses of gut contents of frozen mega-herbivore individuals recovered from permafrost in Northern Siberia and Beringia (Axmanová et al., 2020), furthermore, indicates that they consumed woody as well as herbaceous material, leading to an inference that they occupied landscapes with mosaics of grasslands, shrublands and woodlands. This suggests that ShT which, despite being dominated by the BESh PFT, has a C3G carbon mass per unit area >50% higher than Tun, and a total carbon mass per unit area two orders of magnitude greater than Tun and an order of magnitude greater than St, may have provided suitable habitat for these creatures. Furthermore, ShT was extensive during the glacials, especially in Eurasia, and much more extensive than either Tun or St (Figures 5 & 6). As illustrated in Figure 4, vegetation patterns in eastern Siberia differ between the LIG and Holocene, reflecting the quantitatively different climatic forcing that in turn leads to differences in simulated climatic conditions and patterns. Strikingly, there is a generally greater regional extent of ShT during the LIG than the Holocene. Whether or not the climatic and resulting vegetation differences alone are sufficient to explain persistence of Pleistocene mega-herbivores during the LIG but not the Holocene remains contentious, but our simulations provide additional support for a key role of vegetation differences.

Our third question addressed the nature and extent of vegetation responses in tropical latitudes and the Southern Hemisphere to last glacial stage millennial climatic fluctuations. As illustrated in Figure 3, and described above, although the most striking vegetation responses were simulated in Europe and Eurasia, substantial responses of tropical and Southern Hemisphere vegetation were also simulated. Our results also show that both the magnitude and spatial patterns of these responses differ depending upon the state of the orbital forcing when the shift between stadial and inter-stadial conditions occurs. Overall, our simulations indicate that vegetation patterns in most tropical and Southern Hemisphere land areas were likely markedly affected by millennial climatic fluctuations during the last glacial, although there were localized exceptions to this generalization, including New Zealand, south-east Australia and Tasmania (Figure 3).

The extent to which LIG vegetation patterns paralleled those of the Holocene was the subject of our fourth question. As discussed above and illustrated in Figure 4, whilst there are, as expected, broad similarities, there are also numerous differences both regionally and in terms of the temporal evolution of the vegetation patterns during the two interglacials. Furthermore, these differences are neither restricted to nor most striking in higher latitudes of the Northern Hemisphere, but are obvious on all vegetated continents. Once again, it is the climatic consequences of the quantitatively different forcing that underlie the differences in simulated spatial patterns and temporal evolution of the vegetation. Both the greater magnitude of the Northern Hemisphere insolation peak, and the higher $[CO_2]_{atm}$, at the onset of the LIG than at the onset of the Holocene (Figure 7) resulted not just in globally warmer conditions (Fischer et al., 2018), but in regional differences in climatic conditions and climatic evolution that are reflected by the simulated vegetation differences.

Finally, we asked how similar were global vegetation patterns at the PGM and LGM. Figure 5 illustrates our biome simulations for

the LGM (21 ka) and PGM (140 ka), showing marked differences in many regions; these differences were described above. Once again the quantitatively different forcing, principally the more extreme Northern Hemisphere summer insolation minimum at 140 ka than at 21 ka, leads to differences in simulated climatic conditions that in turn result in the differences in biome patterns. Thus, as with the Holocene and LIG, climate, and the resulting extent and distribution of biomes, differed between the LGM and PGM.

5 | CONCLUSIONS

Firstly, as palaeovegetation records from various parts of the world show, regional vegetation patterns during the LIG differed from those of the Holocene (e.g. Fréchette, Wolfe, Miller, Richard, & de Vernal, 2006; Herring & Gavin, 2015; Kershaw et al., 2007; van der Hammen & Hooghiemstra, 2003; Whitlock, Sarna-Wojcicki, Bartlein, & Nickmann, 2000). However, the timing of some key regional contrasts between the two interglacials differs in our simulations, drawing attention to the difficulty of independently dating terrestrial records of the LIG, and hence of demonstrating such diachronous patterns using palaeovegetation records. Thus, for example, whereas the northernmost extension of BENF in western Siberia is simulated to occur around the middle of the LIG (see Figure 4d, 118 ka), the greatest reduction in the extent of Des in the Sahara, Arabia and the Indian sub-continent is simulated early in the LIG (see Figure 4b, 126 ka). Testing these model-generated hypotheses awaits advances in dating and new records from these regions.

Secondly, simulated biome patterns also differ between the last and penultimate glacial maxima, emphasizing the more general conclusion that, although orbital forcing has a series of characteristic frequencies, the forcing is not strictly cyclic. Thus, no two time slices have identical forcing; hence, no two have identical climate or biome patterns. Although fewer palaeovegetation records are available spanning glacials than interglacials, where such records are available they accord with this conclusion, each warmer or colder interval having similar but not identical vegetation, see, for example Ioannina (Roucoux, Tzedakis, Lawson, & Margari, 2011; Tzedakis, 1994) and Lago Grande di Monticchio (Allen & Huntley, 2009; Allen et al., 2000; Allen, Watts, McGee, & Huntley, 2002).

Thirdly, last glacial stage millennial climatic fluctuations, previously shown to be likely to have strongly influenced vegetation in Eurasia (Huntley, Allen, Collingham, et al., 2013) and biome patterns in southern Africa (Huntley et al., 2016), had widespread effects on global vegetation patterns in the tropics and Southern Hemisphere, as well as on Northern Hemisphere vegetation, and on global carbon budgets. For some biomes, most notably TrEF, climatic conditions simulated by climate model experiments designed to mimic Heinrich Events had a larger impact upon the simulated global extent of the biome than did the overall orbitally forced glacial–interglacial cycle of climatic conditions (Figure 6).

Fourthly, most of Earth's land surface has experienced at least one, and in many regions multiple, biome changes since 140 ka. Primary exceptions are the core areas of TrEF, although the extent of TrEF in each of its principal centres, South America, sub-Saharan Africa and south-east Asia, is nonetheless simulated to have varied substantially, with marked reductions in extent at some times in all three regions.

Despite being in general accord with palaeovegetation evidence, one striking feature that our simulations do not show is a vegetated Sahara during either the early Holocene or LIG, thus conflicting with inferences of a 'green' Sahara at these times on the basis of geomorphic and fossil evidence (Larrasoaña, Roberts, & Rohling, 2013). Although all modelling studies show an enhanced West African monsoon during the early Holocene, they struggle to simulate the magnitude of change; this is a general challenge in palaeoclimatic modelling (Valdes, 2011). Early modelling studies suggested that without incorporation of the strong land surface to atmosphere feedbacks as the vegetation zones expand in response to enhanced monsoon precipitation, climate models are unable to generate sufficient precipitation in the Sahara to support the early Holocene 'greening' (Claussen & Gayler, 1997; de Noblet-Ducoudre, Claussen, & Prentice, 2000). However, this result was not replicated by fully coupled atmosphere–ocean–vegetation models participating in PMIP2 and PMIP3, including HadCM3 with TRIFFID (Braconnot et al., 2012; Harrison et al., 2014). Recent climate model simulations suggest that changes in dust could also be important (Pausata, Messori, & Zhang, 2016), although this result may have been an artefact of that particular model (Hopcroft & Valdes, 2019; Thompson, Skinner, Poulsen, & Zhu, 2019). A lack of sensitivity of modelled vegetation to rainfall in sub-Saharan Africa may also contribute to the problem (Hopcroft, Valdes, Harper, & Beerling, 2017).

Notwithstanding this limitation, this series of palaeovegetation maps simulated for the past 140 kyr (Supplementary Information – Slideshow) provides valuable insights into likely changes in the extent and location of biomes worldwide. As such, it represents a valuable new resource for investigations into the role of environmental history, whether in the origins of present biodiversity patterns (Colville et al., in press), in relation to pre-historic megafaunal extinctions, or in relation to the biogeographical history of anatomically modern humans.

ACKNOWLEDGEMENTS

BH, JRMA, JSS, TH and MF were supported by a Leverhulme Trust Research Grant to BH (RPG-2014-338). Henk Slim provided invaluable support to JRMA and BH in their use of the Durham University High Performance Computing Facility that was used to perform the LPJ-GUESS simulations and associated computation. Yvonne Collingham provided key support with respect to generating the climatic anomalies required to run LPJ-GUESS from the HadCM3 outputs, and also generated the estimates of 'present' climate for shelf grid cells exposed at the LGM. HadCM3 simulations were performed on the facilities of the Advanced Computing Research Centre at the University of Bristol (http://www.bris.ac.uk/acrc/). We are extremely grateful for very helpful comments from Jack Williams, and

for those of an anonymous referee, on our initial submission that enabled us greatly to improve the paper.

DATA AVAILABILITY STATEMENT

The following files have been deposited in the Data Dryad repository: (a) 89 pairs of files in.csv format, one pair for each time slice, including the 'present', each pair comprising one file each for the LPJ-GUESS simulated LAI and C-Mass values for all half-degree grid cells. (b) One.csv format file giving the biome assignments for all 89 time slices for all half-degree grid cells. (c) One ascii fixed format file giving, for all half-degree grid cells, the total area of each grid cell and the % ice-free land area of that grid cell for each of the 89 time slices. (d) Four sets of ArcGIS ascii grid files for a 6-min grid. The first three sets are binary masks for: (i) ice; (ii) ocean; and (iii) land; and the fourth set is quantitative ice-fraction (% ice cover). Each set comprises one file for each of the 89 time slices. and (e) A metadata file describing the contents and formats of these data files.

ORCID


Brian Huntley https://orcid.org/0000-0002-3926-2257

REFERENCES

Allen, J. R. M., Brandt, U., Brauer, A., Hubberten, H., Huntley, B., Keller, J., … Zolitschka, B. (1999). Rapid environmental changes in southern Europe during the last glacial period. *Nature*, *400*, 740–743. https://doi.org/10.1038/23432

Allen, J. R. M., & Huntley, B. (2009). Last interglacial palaeovegetation, palaeoenvironments and chronology: A new record from Lago Grande di Monticchio, southern Italy. *Quaternary Science Reviews*, *28*, 1521–1538. https://doi.org/10.1016/j.quascirev.2009.02.013

Allen, J. R. M., Watts, W. A., & Huntley, B. (2000). Weichselian palynostratigraphy, palaeovegetation and palaeoenvironment: The record from Lago Grande di Monticchio, southern Italy. *Quaternary International*, *73*(74), 91–110. https://doi.org/10.1016/S1040-6182(00)00067-7

Allen, J. R. M., Watts, W. A., McGee, E., & Huntley, B. (2002). Holocene environmental variability – The record from Lago Grande di Monticchio, Italy. *Quaternary International*, *88*, 69–80. https://doi.org/10.1016/S1040-6182(01)00074-X

Andrews, J. T. (1998). Abrupt changes (Heinrich events) in late Quaternary North Atlantic marine environments: A history and review of data and concepts. *Journal of Quaternary Science*, *13*, 3–16. https://doi.org/10.1002/(SICI)1099-1417(199801/02)13:1<3:AID-JQS361>3.0.CO;2-0

Axmanová, I., Robovský, J., Tichý, L., Danihelka, J., Troeva, E., Protopopov, A., & Chytrý, M. (2020). Habitats of Pleistocene megaherbivores reconstructed from the frozen fauna remains. *Ecography*, *43*(5), 703–713. https://doi.org/10.1111/ecog.04940

Bauska, T. K., Brook, E. J., Marcott, S. A., Baggenstos, D., Shackleton, S., Severinghaus, J. P., & Petrenko, V. V. (2018). Controls on millennial-scale atmospheric CO_2 variability during the last glacial period. *Geophysical Research Letters*, *45*, 7731–7740.

Bereiter, B., Eggleston, S., Schmitt, J., Nehrbass-Ahles, C., Stocker, T. F., Fischer, H., … Chappellaz, J. (2015). Revision of the EPICA Dome C CO_2 record from 800 to 600kyr before present. *Geophysical Research Letters*, *42*, 542–549.

Braconnot, P., Harrison, S. P., Kageyama, M., Bartlein, P. J., Masson-Delmotte, V., Abe-Ouchi, A., … Zhao, Y. (2012). Evaluation of climate models using palaeoclimatic data. *Nature Climate Change*, *2*, 417–424. https://doi.org/10.1038/nclimate1456

Brauer, A., Allen, J. R. M., Mingram, J., Dulski, P., Wulf, S., & Huntley, B. (2007). Evidence for last interglacial chronology and environmental change from Southern Europe. *Proceedings of the National Academy of Sciences of the United States of America*, *104*, 450–455. https://doi.org/10.1073/pnas.0603321104

Claussen, M., & Gayler, V. (1997). The greening of the Sahara during the mid-Holocene: Results of an interactive atmosphere-biome model. *Global Ecology and Biogeography Letters*, *6*, 369–377. https://doi.org/10.2307/2997337

Colville, J. F., Beale, C. M., Forest, F., Altwegg, R., Huntley, B., & Cowling, R. M. (in press). Plant richness, turnover and evolutionary diversity track gradients of stability and ecological opportunity in a megadiversity centre. *Proceedings of the National Academy of Sciences of the United States of America*.

Cox, P. M. (2001). Description of the "TRIFFID" dynamic global vegetation model. Hadley Centre, Met Office. Hadley Centre Technical Note, 24. 16 pp. M.O. Hadley Centre, Bracknell, Berks.

Davies-Barnard, T., Ridgwell, A., Singarayer, J., & Valdes, P. (2017). Quantifying the influence of the terrestrial biosphere on glacial-interglacial climate dynamics. *Climate of the Past*, *13*, 1381–1401. https://doi.org/10.5194/cp-13-1381-2017

de Boer, B., van de Wal, R. S. W., Lourens, L. J., Bintanja, R., & Reerink, T. J. (2013). A continuous simulation of global ice volume over the past 1 million years with 3-D ice-sheet models. *Climate Dynamics*, *41*, 1365–1384. https://doi.org/10.1007/s00382-012-1562-2

de Noblet-Ducoudre, N., Claussen, R., & Prentice, C. (2000). Mid-Holocene greening of the Sahara: First results of the GAIM 6000 year BP Experiment with two asynchronously coupled atmosphere/biome models. *Climate Dynamics*, *16*, 643–659. https://doi.org/10.1007/s003820000074

EPICA Community Members. (2004). Eight glacial cycles from an Antarctic ice core. *Nature*, *429*, 623–628.

Fischer, H., Meissner, K. J., Mix, A. C., Abram, N. J., Austermann, J., Brovkin, V., … Zhou, L. (2018). Palaeoclimate constraints on the impact of 2 °C anthropogenic warming and beyond. *Nature Geoscience*, *11*, 474–485. https://doi.org/10.1038/s41561-018-0146-0

Forrest, M., Eronen, J. T., Utescher, T., Knorr, G., Stepanek, C., Lohmann, G., & Hickler, T. (2015). Climate-vegetation modelling and fossil plant data suggest low atmospheric CO_2 in the late Miocene. *Climate of the Past*, *11*, 1701–1732.

Fréchette, B., Wolfe, A. P., Miller, G. H., Richard, P. J. H., & de Vernal, A. (2006). Vegetation and climate of the last interglacial on Baffin Island, Arctic Canada. *Palaeogeography Palaeoclimatology Palaeoecology*, *236*, 91–106. https://doi.org/10.1016/j.palaeo.2005.11.034

Guetter, P. J., & Kutzbach, J. E. (1990). A modified Köppen classification applied to model simulations of glacial and interglacial climates. *Climatic Change*, *16*, 193–215.

Harris, I., Jones, P. D., Osborn, T. J., & Lister, D. H. (2014). Updated high-resolution grids of monthly climatic observations – The CRU TS3.10 Dataset. *International Journal of Climatology*, *34*, 623–642. https://doi.org/10.1002/joc.3711

Harrison, S. P., Bartlein, P. J., Brewer, S., Prentice, I. C., Boyd, M., Hessler, I., … Willis, K. (2014). Climate model benchmarking with glacial and mid-Holocene climates. *Climate Dynamics*, *43*, 671–688. https://doi.org/10.1007/s00382-013-1922-6

Haxeltine, A., & Prentice, I. C. (1996). BIOME3: An equilibrium terrestrial biosphere model based on ecophysiological constraints, resource availability and competition among plant functional types. *Global Biogeochemical Cycles*, *10*, 693–710. https://doi.org/10.1029/96GB02344

Herring, E. M., & Gavin, D. G. (2015). Climate and vegetation since the Last Interglacial (MIS 5e) in a putative glacial refugium, northern Idaho, USA. *Quaternary Science Reviews*, *117*, 82–95. https://doi.org/10.1016/j.quascirev.2015.03.028

Hopcroft, P. O., & Valdes, P. J. (2019). On the role of dust-climate feedbacks during the mid-Holocene. *Geophysical Research Letters*, *46*, 1612–1621. https://doi.org/10.1029/2018GL080483

Hopcroft, P. O., Valdes, P. J., Harper, A. B., & Beerling, D. J. (2017). Multi vegetation model evaluation of the Green Sahara climate regime. *Geophysical Research Letters*, *44*, 6804–6813. https://doi.org/10.1002/2017GL073740

Huntley, B., Allen, J. R. M., Barnard, P., Collingham, Y. C., & Holliday, P. R. (2013). Species' distribution models indicate contrasting late-Quaternary histories for southern and northern hemisphere bird species. *Global Ecology and Biogeography*, *22*, 277–288. https://doi.org/10.1111/j.1466-8238.2011.00751.x

Huntley, B., Allen, J. R. M., Collingham, Y. C., Hickler, T., Lister, A. M., Singarayer, J., … Valdes, P. J. (2013). Millennial climatic fluctuations are key to the structure of last glacial ecosystems. *PLoS One*, *8*, e61963. https://doi.org/10.1371/journal.pone.0061963

Huntley, B., Collingham, Y. C., Singarayer, J. S., Valdes, P. J., Barnard, P., Midgley, G. F., … Ohlemüller, R. (2016). Explaining patterns of avian diversity and endemicity: Climate and biomes of southern Africa over the last 140,000 years. *Journal of Biogeography*, *43*, 874–886.

Jolly, D., Prentice, I. C., Bonnefille, R., Ballouche, A., Bengo, M., Brenac, P., … Waller, M. (1998). Biome reconstruction from pollen and plant macrofossil data for Africa and the Arabian peninsula at 0 and 6000 years. *Journal of Biogeography*, *25*, 1007–1027. https://doi.org/10.1046/j.1365-2699.1998.00238.x

Jouzel, J., Masson-Delmotte, V., Cattani, O., Dreyfus, G., Falourd, S., Hoffmann, G., … Wolff, E. W. (2007). Orbital and millennial Antarctic climate variability over the past 800,000 years. *Science*, *317*, 793–796. https://doi.org/10.1126/science.1141038

Kershaw, A. P., McKenzie, G. M., Porch, N., Roberts, R. G., Brown, J., Heijnis, H., … Newallt, P. R. (2007). A high-resolution record of vegetation and climate through the last glacial cycle from Caledonia Fen, southeastern highlands of Australia. *Journal of Quaternary Science*, *22*, 481–500. https://doi.org/10.1002/jqs.1127

Larrasoaña, J. C., Roberts, A. P., & Rohling, E. J. (2013). Dynamics of green Sahara periods and their role in hominin evolution. *PLoS One*, *8*, e76514. https://doi.org/10.1371/journal.pone.0076514

Laskar, J., Robutel, P., Joutel, F., Gastineau, M., Correia, A. C. M., & Levrard, B. (2004). A long-term numerical solution for the insolation quantities of the Earth. *Astronomy & Astrophysics*, *428*, 261–285.

Loulergue, L., Schilt, A., Spahni, R., Masson-Delmotte, V., Blunier, T., Lemieux, B., … Chappellaz, J. (2008). Orbital and millennial-scale features of atmospheric CH_4 over the past 800,000 years. *Nature*, *453*, 383–386.

Luthi, D., Le Floch, M., Bereiter, B., Blunier, T., Barnola, J. M., Siegenthaler, U., … Stocker, T. F. (2008). High-resolution carbon dioxide concentration record 650,000–800,000 years before present. *Nature*, *453*, 379–382.

Marchant, R., Cleef, A., Harrison, S. P., Hooghiemstra, H., Markgraf, V., van Boxel, J., … Wille, M. (2009). Pollen-based biome reconstructions for Latin America at 0, 6000 and 18 000 radiocarbon years ago. *Climate of the Past*, *5*, 725–767. https://doi.org/10.5194/cp-5-725-2009

Miller, P. A., Giesecke, T., Hickler, T., Bradshaw, R. H. W., Smith, B., Seppa, H., … Sykes, M. T. (2008). Exploring climatic and biotic controls on Holocene vegetation change in Fennoscandia. *Journal of Ecology*, *96*, 247–259. https://doi.org/10.1111/j.1365-2745.2007.01342.x

Nolan, C., Overpeck, J. T., Allen, J. R. M., Anderson, P. M., Betancourt, J. L., Binney, H. A., … Jackson, S. T. (2018). Past and future global transformation of terrestrial ecosystems under climate change. *Science*, *361*, 920–923. https://doi.org/10.1126/science.aan5360

Olson, D. M., Dinerstein, E., Wikramanayake, E. D., Burgess, N. D., Powell, G. V. N., Underwood, E. C., … Kassem, K. R. (2001). Terrestrial ecoregions of the world: A new map of life on Earth. *BioScience*, *51*, 933–938. https://doi.org/10.1641/0006-3568(2001)051[0933:TEOTWA]2.0.CO;2

Olson, J., Watts, J. A., & Allison, L. J. (1983). Carbon in live vegetation of major world ecosystems. Oak Ridge National Laboratory, ORNL-5862.

Parrenin, F., Barnola, J. M., Beer, J., Blunier, T., Castellano, E., Chappellaz, J., … Wolff, E. (2007). The EDC3 chronology for the EPICA dome C ice core. *Climate of the Past*, *3*, 485–497. https://doi.org/10.5194/cp-3-485-2007

Pausata, F. S. R., Messori, G., & Zhang, Q. (2016). Impacts of dust reduction on the northward expansion of the African monsoon during the Green Sahara period. *Earth and Planetary Science Letters*, *434*, 298–307. https://doi.org/10.1016/j.epsl.2015.11.049

Peltier, W. R. (2004). Global glacial isostasy and the surface of the ice-age earth: The ICE-5G (VM2) model and GRACE. *Annual Review of Earth and Planetary Sciences*, *32*, 111–149. https://doi.org/10.1146/annurev.earth.32.082503.144359

Petit, J. R., Jouzel, J., Raynaud, D., Barkov, N. I., Barnola, J.-M., Basile, I., … Stievenard, M. (1999). Climate and atmospheric history of the past 420,000 years from the Vostok ice core, Antarctica. *Nature*, *399*, 429–436. https://doi.org/10.1038/20859

Prentice, I. C., Cramer, W., Harrison, S. P., Leemans, R., Monserud, R. A., & Solomon, A. M. (1992). A global biome model based on plant physiology and dominance, soil properties and climate. *Journal of Biogeography*, *19*, 117–134.

Prentice, I. C., Harrison, S. P., & Bartlein, P. J. (2011). Global vegetation and terrestrial carbon cycle changes after the last ice age. *New Phytologist*, *189*, 988–998. https://doi.org/10.1111/j.1469-8137.2010.03620.x

Rasmussen, S. O., Bigler, M., Blockley, S. P., Blunier, T., Buchardt, S. L., Clausen, H. B., … Winstrup, M. (2014). A stratigraphic framework for abrupt climatic changes during the Last Glacial period based on three synchronized Greenland ice-core records: Refining and extending the INTIMATE event stratigraphy. *Quaternary Science Reviews*, *106*, 14–28. https://doi.org/10.1016/j.quascirev.2014.09.007

Roucoux, K. H., Tzedakis, P. C., Lawson, I. T., & Margari, V. (2011). Vegetation history of the penultimate glacial period (Marine Isotope Stage *6*) at Ioannina, north-west Greece. *Journal of Quaternary Science*, *26*, 616–626. https://doi.org/10.1002/jqs.1483

Scheiter, S., & Higgins, S. I. (2009). Impacts of climate change on the vegetation of Africa: An adaptive dynamic vegetation modelling approach. *Global Change Biology*, *15*, 2224–2246. https://doi.org/10.1111/j.1365-2486.2008.01838.x

Sher, A. (1997). Late-Quaternary extinction of large mammals in northern Eurasia: A new look at the Siberian contribution. In B. Huntley, W. Cramer, A. V. Morgan, H. C. Prentice, & J. R. M. Allen (Eds.), *Past and future rapid environmental changes: The spatial and evolutionary responses of terrestrial biota* (pp. 319–339). Berlin: Springer-Verlag.

Singarayer, J. S., & Valdes, P. J. (2010). High-latitude climate sensitivity to ice-sheet forcing over the last 120 kyr. *Quaternary Science Reviews*, *29*, 43–55.

Smith, B., Prentice, I. C., & Sykes, M. T. (2001). Representation of vegetation dynamics in the modelling of terrestrial ecosystems: Comparing two contrasting approaches within European climate space. *Global Ecology and Biogeography*, *10*, 621–637. https://doi.org/10.1046/j.1466-822X.2001.00256.x

Smith, B., Warlind, D., Arneth, A., Hickler, T., Leadley, P., Siltberg, J., & Zaehle, S. (2014). Implications of incorporating N cycling and N limitations on primary production in an individual-based dynamic vegetation model. *Biogeosciences*, *11*, 2027–2054. https://doi.org/10.5194/bg-11-2027-2014

Tarasov, P. E., Webb III, T., Andreev, A. A., Afanas'eva, N. B., Berezina, N. A., Bezusko, L. G., … Zernitskaya, V. P. (1998). Present-day and mid-Holocene biomes reconstructed from pollen and plant macrofossil data from the former Soviet Union and Mongolia. *Journal of Biogeography*, *25*, 1029–1053. https://doi.org/10.1046/j.1365-2699.1998.00236.x

Thompson, A. J., Skinner, C. B., Poulsen, C. J., & Zhu, J. (2019). Modulation of mid-Holocene African rainfall by dust aerosol direct and indirect effects. *Geophysical Research Letters*, *46*, 3917–3926. https://doi.org/10.1029/2018GL081225

Thonicke, K., Venevsky, S., Sitch, S., & Cramer, W. (2001). The role of fire disturbance for global vegetation dynamics: Coupling fire into a Dynamic Global Vegetation Model. *Global Ecology and Biogeography*, *10*, 661–677. https://doi.org/10.1046/j.1466-822X.2001.00175.x

Tzedakis, P. C. (1994). Vegetation change through glacial-interglacial cycles - a long pollen sequence perspective. *Philosophical Transactions of the Royal Society of London: Series B - Biological Sciences*, *345*, 403–432.

Valdes, P. (2011). Built for stability. *Nature Geoscience*, *4*, 414–416. https://doi.org/10.1038/ngeo1200

Valdes, P. J., Armstrong, E., Badger, M. P. S., Bradshaw, C. D., Bragg, F., Crucifix, M., … Williams, J. H. T. (2017). The BRIDGE HadCM3 family of climate models: HadCM3@Bristol v1.0. *Geoscientific Model Development*, *10*, 3715–3743.

van der Hammen, T., & Hooghiemstra, H. (2003). Interglacial-glacial Fuquene-3 pollen record from Colombia: An Eemian to Holocene climate record. *Global and Planetary Change*, *36*, 181–199. https://doi.org/10.1016/S0921-8181(02)00184-4

Walker, M. J. C., Berkelhammer, M., Björck, S., Cwynar, L. C., Fisher, D. A., Long, A. J., … Weiss, H. (2012). Formal subdivision of the Holocene Series/Epoch: A discussion paper by a working group of INTIMATE (Integration of ice-core, marine and terrestrial records) and the Subcommission on Quaternary Stratigraphy (International Commission on Stratigraphy). *Journal of Quaternary Science*, *27*, 649–659. https://doi.org/10.1002/jqs.2565

Whitlock, C., Sarna-Wojcicki, A. M., Bartlein, P. J., & Nickmann, R. J. (2000). Environmental history and tephrostratigraphy at Carp lake, southwestern Columbia basin, Washington, U.S.A. *Palaeogeography, Palaeoclimatology, Palaeoecology*, *155*, 7–29. https://doi.org/10.1016/S0031-0182(99)00092-9

Williams, J. W., Summers, R. L., & Webb, T. (1998). Applying plant functional types to construct biome maps from eastern North American pollen data: Comparisons with model results. *Quaternary Science Reviews*, *17*, 607–627. https://doi.org/10.1016/S0277-3791(98)00014-6

Wolff, E. W., Chappellaz, J., Blunier, T., Rasmussen, S. O., & Svensson, A. (2010). Millennial-scale variability during the last glacial: The ice core record. *Quaternary Science Reviews*, *29*, 2828–2838. https://doi.org/10.1016/j.quascirev.2009.10.013

BIOSKETCH

Brian Huntley is a palaeoecologist, ecologist and biogeographer with research interests in interactions between species, ecosystems and their changing environment. His work encompasses studies of the palaeoecology and palaeoenvironments of the Quaternary, of present ecosystems and biogeographical patterns, and of the potential impacts of anthropogenic global change on species and ecosystems. His research has considered a range of taxonomic groups, from plants to extinct Quaternary mammals, and various ecosystems, from Arctic tundra to fynbos. He has particular interest in birds and climatic change, and in the development of conservation strategies informed by research into how species and ecosystems respond to environmental changes.

Author contributions: B.H. conceived the study; P.J.V. and J.S.S. performed the palaeoclimate simulations; M.F. and T.H. advised on running the palaeovegetation simulations; MF developed and implemented code to incorporate the climatic anomalies, extend simulations to the shelf areas and specify the varying obliquity; M.F., T.H. and J.R.M.A. parameterized the PFTs; J.R.M.A. performed the palaeovegetation simulations and prepared Figure 6; B.H. developed the biome inference approach and wrote the program to implement this, mapped the simulated biomes, analysed the simulation results, prepared Figures 1–5 and 7, prepared the Supplementary Material and drafted the manuscript. All authors commented upon and contributed to the final version of the manuscript.

SUPPORTING INFORMATION

Additional supporting information may be found online in the Supporting Information section.

How to cite this article: Allen JRM, Forrest M, Hickler T, Singarayer JS, Valdes PJ, Huntley B. Global vegetation patterns of the past 140,000 years. *J Biogeogr*. 2020;00:1–18. https://doi.org/10.1111/jbi.13930

APPENDIX 1

Rule-based biome inference

The biome occupying each grid cell was inferred using the following rules, applied in the order given below where they are expressed in the form of a dichotomous key. The majority of the rules applied relate to the simulated leaf area index (LAI) of one or more plant functional types (PFTs – see Table 1). The initial rule, however, considers the simulated total carbon mass (C-Mass) for the grid cell, relative to a threshold value of 1.0×10^9 kg for a half-degree grid cell at the equator, area 3,087.57 km^2, all of which is ice-free land. The threshold applied to a given grid cell is adjusted to account for its ice-free land area, thus taking into account the reduced areas of grid cells at higher latitudes, of coastal grid cells and of grid cells partially covered by ice sheets.

1.	C-Mass < threshold value†	
2.	LAI BESh = 0.0	1. Desert
2.	LAI BESh > 0.0	2. Tundra
1.	C-Mass ≥ threshold value	
3.	LAI TrBE > 2.0	3. Tropical Evergreen Forest
3.	LAI TrBE ≤ 2.0	
4.	LAI TrBR > 0.6	4. Tropical Raingreen Forest
4.	LAI TrBR ≤ 0.6	
5.	LAI C4G > 0.3	
6.	LAI Tr-shrub > 0.3 **OR** LAI TrBR > 0.3	5. Savanna
6.	LAI Tr-shrub ≤ 0.3 **AND** LAI TrBR ≤ 0.3	6. Tropical Grassland
5.	LAI C4G ≤ 0.3	

7.	LAI TeBS > 1.0	
8.	LAI B-tree > 0.1 **OR** LAI TeNE > 0.1	7. Temperate Mixed Forest
8.	LAI B-tree ≤ 0.1 **AND** LAI TeNE ≤ 0.1	8. Temperate Summergreen Forest
7.	LAI TeBS ≤ 1.0	
9.	LAI TeNE > 1.0	20. Temperate Needle-leaved Evergreen Forest
9.	LAI TeNE ≤ 1.0	
10.	LAI TeBE > 1.0	9. Temperate Broad-leaved Evergreen Forest
10.	LAI TeBE ≤ 1.0	
11.	LAI TeRSh *plus* LAI TeESh > 0.3	
12.	LAI B-tree > 0.02	10. Boreal Parkland
12.	LAI B-tree ≤ 0.02	
13.	LAI TeBS > 0.02	11. Temperate Parkland
13.	LAI TeBS ≤ 0.02	
14.	LAI TeBE > 0.3	12. Warm Temperate Woodland
14.	LAI TeBE ≤ 0.3	
15.	LAI C3G> (LAI TeRSh *plus* LAI TeESh)	21. Semi-desert
15.	LAI C3G ≤ (LAI TeRSh *plus* LAI TeESh)	13. Temperate Shrubland
11.	LAI TeRSh *plus* LAI TeESh ≤ 0.3	
16.	LAI BNE > 0.3	14. Boreal Needle-leaved Evergreen Forest
16.	LAI BNE ≤ 0.3	
17.	LAI BNS > 0.1	
18.	LAI BESh > 1.0	15. Boreal Woodland
18.	LAI BESh ≤ 1.0	16. Boreal Needle-leaved Summergreen Forest
17.	LAI BNS ≤ 0.1	
19.	LAI BIBS > 0.1	17. Boreal Broad-leaved Summergreen Forest
19.	LAI BIBS ≤ 0.1	
20.	LAI BESh > 0.3	18. Shrub Tundra
20.	LAI BESh ≤ 0.3	
21.	LAI C3G > 0.3	19. Steppe
21.	LAI C3G ≤ 0.3	
22.	[(Σ LAI *minus* (LAI C3G *plus* LAI BESh))] ≤ 0.01	2. Tundra
22.	[(Σ LAI *minus* (LAI C3G *plus* LAI BESh))]> 0.01	
23.	[(Σ LAI *minus* (LAI TeBE *plus* LAI C3G *plus* LAI TeESh *plus* LAI TeRSh))] ≤ 0.01	13. Temperate Shrubland
23.	[(Σ LAI *minus* (LAI TeBE *plus* LAI C3G *plus* LAI TeESh *plus* LAI TeRSh))]> 0.01	
24.	LAI TrBE *plus* LAI TrIBE > 1.7	3. Tropical Evergreen Forest
24.	LAI TrBE *plus* LAI TrIBE ≤ 1.7	22. Unclassified

[†]((grid cell area × % ice-free land)/100)/3087·57) x (1·0 × 10^9) kg.